

1 **Title:** Endogenous suspension and reset of consciousness: 7T fMRI brain mapping of the
2 extended cessation meditative endpoint

3

4 **Authors**

5 Winson F.Z. Yang^{1,2}, ⁺Akila Kadambi^{3,4}, ⁺Kilian Abellana-Pérez^{5,6}, Grace Mackin^{1,2,7}, Isidora
6 Beslic^{1,2,7}, Ruby Potash^{1,2}, Terje Sparby^{8,9,10}, Matthew D. Sacchet^{1,2*}
7 (meditationadministration@mgh.harvard.edu)

8

9 ⁺Denotes co-second-authors

10

11 **Affiliations**

12 ¹Meditation Research Program, Department of Psychiatry, Massachusetts General Hospital,
13 Harvard Medical School, Boston, USA

14 ²Athinoula A. Martinos Center for Biomedical Imaging, Department of Radiology,
15 Massachusetts General Hospital, Harvard Medical School, USA

16 ³Dept. of Psychiatry and Biobehavioral Sciences, David Geffen School of Medicine, University
17 of California, Los Angeles, USA

18 ⁴Brain and Creativity Institute, Dornsife College of Letters, Arts, and Sciences, University of
19 Southern California, Los Angeles, USA

20 ⁵Institut Guttmann, Institut Universitari de Neurorehabilitació adscrit a la Universitat Autònoma
21 de Barcelona, Badalona, Spain

22 ⁶Department of Medicine, Faculty of Medicine and Health Sciences, Institute of Neurosciences,
23 University of Barcelona, Barcelona, Spain

24 ⁷Northeastern University, Boston, USA

25 ⁸Steiner University College, 0260 Oslo, Norway

26 ⁹Department of Psychology and Psychotherapy, Witten/Herdecke University, 58455 Witten,
27 Germany

- 28 ¹⁰Integrated Curriculum for Anthroposophic Psychology, Witten/Herdecke University, 58455
29 Witten, Germany

30 **Abstract**

31 Extended cessation (EC), an advanced meditative state in which consciousness is volitionally
32 suspended and later reset with immense mental clarity, equanimity, and peace, offers an
33 endogenous model for investigating the mechanisms of consciousness. Using ultra-high-
34 resolution 7T fMRI with dense within-subject sampling (N=3), we quantified whole-brain
35 activity, functional and effective connectivity, cortical gradients, and eigenmodes, and related
36 them to chemoarchitecture and cognitive maps. EC is marked by increased activity in unimodal
37 regions, down-regulation in transmodal regions, subcortex, and brainstem, an expansion of the
38 principal gradient, and decrease in low-order global eigenmodes. Cognitive decoding linked EC
39 to heightened perceptual clarity and attention, least with mental suffering, and co-varied with
40 histaminergic H₁ receptors topology. These findings challenge predictions of Global Neuronal
41 Workspace and Integrated Information Theory, while supporting the Active Inference
42 Framework. More broadly, EC demonstrates that consciousness can cease without global
43 suppression, suggesting a potential “reset” mechanism that fosters equanimity and the potential
44 for flourishing.

45

46 **Keywords:** advanced meditation, extended cessation, consciousness, subcortical, brainstem,
47 functional connectivity, chemoarchitecture

48

49 **Introduction**

50 In most scientific and clinical frameworks, wakefulness is assumed to entail ongoing
51 subjective consciousness¹. Advanced meditative states challenge this assumption by showing
52 that consciousness can be radically thinned to minimal ‘content-free’ awareness^{2,3} or even
53 entirely suspended momentarily⁴⁻⁷ or for an extended duration⁸. These findings highlight the
54 extraordinary plasticity of consciousness, raising fundamental questions for theories of
55 consciousness, including Global Neuronal Workspace, Integrated Information Theory, and
56 Active Inferences Framework, and their relevance to human flourishing^{9,10}.

57 Advanced meditation situates these rare states within a broader scientific agenda:
58 understanding consciousness as a trainable and reconfigurable capacity across meditative
59 development^{11,12}. This systematic mental training can lead to meditative endpoints, variously
60 described as “awakening”^{13,14}, “beatitude”¹⁵, “salvation”¹⁶, or “enlightenment”^{13,14}, that entail
61 profound shifts in perception, emotion, and self-processing. Studying such endpoints offers not
62 only a natural experiment for testing theories of consciousness but also insights into how such
63 they can induce a “reset” of consciousness that fosters equanimity, resilience, and well-being, all
64 of which are critical priorities in global mental health¹⁷⁻¹⁹.

65 Here, we study extended cessation (EC), a rare meditative endpoint where practitioners
66 report temporary suspensions of ordinary consciousness and mental activities^{4,8}. EC can vary
67 from minutes to days, is entered and exited volitionally, and is frequently followed by profound
68 psychological aftereffects, including extreme sense of relief, clarity, openness, peace,
69 equanimity, heightened sensory sensitivity, significant reduction in mental suffering, reduced
70 repetitive thoughts, stoppage of negative self-talk, and an absence of inner narration^{8,18,19}. Unlike
71 non-conscious states induced by pharmacological agents (e.g., anesthesia or psychedelics)^{20,21},
72 EC is unique in being endogenous, reversible, precisely timed, and followed by heightened well-
73 being, making it an excellent natural experiment for probing the mechanisms of consciousness.
74 One canonical form of EC found in Theravada Buddhism is Nirodha Samāpatti^{8,22-24}. Here, we
75 investigate the broader neurobiological principles of EC without making definitive claims about
76 its doctrinal interpretation^{4,6,7}. Please refer to Laukkonen et al. for a recent discussion of the
77 historical and theoretical context of Nirodha Samāpatti⁸. It is noteworthy that Nirodha Samāpatti

78 is considered to be among the highest, or the highest, meditative attainment in some
79 interpretations of Theravada Buddhism^{25,26}.

80 From a neuroscience perspective, studying EC offers a powerful opportunity to explore
81 the fundamental nature and mechanisms of consciousness. A central limitation in current
82 consciousness research is the absence of an endogenous and reversible method to suspend
83 awareness while preserving physiological stability^{20,21} and enabling prospectively timed re-
84 emergence^{8,23}. EC addresses this gap^{7,8}. Compared to sleep, anesthesia, and disorders of
85 consciousness, EC constitutes a fourth experimental context in its uniqueness self-initiate and
86 control consciousness. This enables precise examination of transition dynamics at entry and exit
87 and the mechanisms that dismantle and reinstate conscious access. Additionally, the notable
88 aftereffects of EC described above may relate to significant neuroplasticity and reorganization of
89 the brain, potentially informing techniques to enhance cognitive function, emotional regulation,
90 overall wellbeing and happiness, and thriving.

91 Current competing frameworks of consciousness make testable predictions for EC.
92 Global Neuronal Workspace (GNW) predicts a collapse of long-range connectivity and reduced
93 feedback connectivity during suspension of consciousness²⁷ while Integrated Information Theory
94 (IIT) predicts a decrease in network differentiation during non-conscious states²⁸. In contrast, the
95 Active Inference Framework (AIF) predicts down-weighting of sensory precision via thalamo-
96 cortical gating during non-conscious states²⁹. The distinct features of EC allow comparison
97 among theories about how consciousness is represented and suspended in the human brain.

98 Here we present the first neuroscientific, empirical investigation of EC, using ultra-high-
99 resolution 7T functional magnetic resonance imaging (fMRI) to investigate the whole-brain
100 activity, connectivity, and causal dynamics of network organization during EC. The ultra-high
101 spatial resolution of 7T imaging allows for precise measurement of small but critical brain
102 structures that are central to consciousness and arousal regulation, such as the thalamus,
103 brainstem, and subcortical nuclei. This methodology is particularly powerful for the study of
104 consciousness, where transitions between conscious and non-conscious brain states may be
105 mediated by subtle shifts in deep-brain activity. Moreover, we used a novel and systematic

106 neurophenomenological approach to rigorously examine the subjective experience of EC,
107 enabling a rare convergence of first-person insight and third-person measurement.

108 This study provides important initial evidence for the neuroscience of EC and related
109 fundamental aspects of consciousness, with potential therapeutic implications for human
110 flourishing. In this study we sought to answer three key questions: (1) What brain
111 reconfiguration accompanies voluntary suspension of consciousness?; (2) What are the causal
112 brain dynamics of EC?; and (3) Which neurochemical systems are implicated, as inferred from
113 spatial coupling to normative receptor distributions?

114 Our findings indicate that consciousness can be suspended without global cortical
115 suppression. During EC, unimodal systems (e.g., visual and dorsal-attention networks) remain
116 selectively engaged while transmodal hubs and thalamo-striatal circuits are down-regulated; the
117 principal cortical gradient polarizes rather than flattens; and network–neurochemical coupling
118 aligns with histaminergic (H \square) precision control of sensory gating. Meta-analytic decoding
119 demonstrated that EC is functionally aligned with perception and attention, while being least
120 associated with mental suffering and distress. This neuronal signature is most consistent with
121 AIF, constrains GNW theory, and challenges IIT. This study demonstrates that the human brain
122 can volitionally dismantle and reassemble conscious processing, offers a radical model for
123 testing theories of consciousness, and highlights the possibility that consciousness can ‘reset’ and
124 orient toward equanimity and flourishing.

125 **Results**

126 *EC Phenomenology*

127 Detailed demographic of participants (N = 3) are provided in Methods. Participant
128 endorsement of EC phenomenology is presented in **Fig. 1**. Here, we summarize the key
129 phenomenology for the setup, entry, exit, and afterglow of EC.

130 **Setup.** Participants typically used advanced absorption concentration meditation (ACAM)
131 to set up EC. ACAM is a series of meditative absorption states accompanied by blissful
132 sensations, emotional happiness, and equanimity, followed by an increasing reduction of input
133 from the physical environment and the reduction of contents of consciousness to a bare minimum

134 experience. One participant who had previously trained using ACAM for setup, no longer
135 necessarily needed ACAM to enter EC. Additionally, all but one participant incorporated
136 elements of advanced investigative insight meditation (AIIM), that is, a neutral observation of
137 phenomena, as part of their preparatory routine for EC.

138 **Onset.** All participants reported that internal verbalization (thinking), body sensations,
139 and feeling ceased during the onset of EC. With one exception, participants reported no primary
140 experiential emphasis on either incongruence, transient nature of experience, or self-lessness
141 (these are typically present during momentary cessations).

142 **EC.** During EC, participants reported that typically all consciousness experience was
143 completely offline.

144 **Exit.** Upon emerging from EC, all participants reported that biographical memory and
145 ego-centered cognitive processing were typically absent, and they did not perceive any
146 separation between themselves and the environment. All participants reported a vivid clarity of
147 mind and an experience of objectless awareness. All but one participant reported the return of
148 mental activity in a specific sequence: first thought, then bodily sensation, and finally internal
149 verbalization.

150 **Afterglow.** After EC, all participants reported typically experiencing intense sensory
151 vividness, accompanied by a strong and lasting peace. They all also reported typically being
152 inclined to solitude, and many described a deep, abiding joy.

153 ***Brain activity during EC: Regional homogeneity (ReHo)***

154 Comprehensive results/summary tables of significant regions are included in the
155 **Supplementary excel file**. Results are visualized in **Fig. 2**. Here, we only provide a summary of
156 the results.

157 ***Across both counting and memory control conditions.*** In the cortex, EC, compared to
158 both counting and memory conditions, was associated with higher ReHo values in the bilateral
159 visual and posterior cortices, frontal eye fields, temporal poles, left prefrontal, parietal, temporal
160 cortices, and right dorsomedial prefrontal cortex; and lower ReHo values in the bilateral

161 prefrontal, somatomotor, temporal, and orbitofrontal cortices, posterior frontal opercula and
162 insula, left precuneus-posterior cingulate cortex, and right cingulate cortex.

163 In the subcortex, EC was primarily associated with decreased ReHo values. Regions
164 include the ventoposterior (THA-VP) and right dorsoanterior (THA-DA) thalamus, left anterior
165 putamen, right hippocampus, medial amygdala, anterior caudate, and globus pallidus. Increased
166 ReHo was also seen in the left hippocampus, medial amygdala, and shell of the nucleus
167 accumbens.

168 In the brainstem, EC was associated with higher ReHo values in the median raphe, raphe
169 obscurus, left inferior medullary reticular formation (MRt), mesencephalic reticular formation,
170 inferior olivary nucleus, viscerosensory-motor nuclei complex, right alpha part of the
171 parvocellular reticular nucleus, superior MRt, and superior olivary complex. EC was also
172 associated with lower ReHo values in the dorsal raphe, left locus coeruleus, subcoeruleus,
173 laterodorsal tegmental nucleus-central gray of the rhombencephalon, right cuneiform nucleus,
174 superior colliculus, and parabrachial pigmented nucleus complexes of the ventral tegmental area
175 (VTA-PBP).

176 In the cerebellum, EC was associated with higher ReHo values in cerebellum regions 6
177 (divided attention) and 10 (autobiographical recall and interference resolution).

178 Additional significant regions of interest (ROIs) for each control condition are presented
179 below.

180 ***EC vs counting control condition.*** Additionally, EC, compared to the counting control
181 condition, was associated with lower ReHo values in the left dorsoposterior thalamus (THA-DP),
182 raphe magnus, left substantia nigra, and red nucleus.

183 ***EC vs memory control condition.*** In the subcortex, EC compared to the memory control
184 condition, was associated with higher ReHo values in the left posterior globus pallidus and
185 putamen, and right nucleus accumbens. Decreased ReHo values were found in the bilateral
186 lateral amygdala and right ventroanterior (THA-VA) thalamus and THA-VP. In the brainstem,
187 higher ReHo values were found in the left isthmus reticular formation, pedunculotegmental
188 nucleus, superior MRt, and right medial parabrachial nucleus; and lower ReHo values in the right

189 inferior olivary nucleus and microcellular tegmental nucleus – prabigeminal nucleus. In the
190 cerebellum, EC, compared to the memory control condition, was associated with lower ReHo in
191 the cerebellar region 4 (associated with action observation).

192 Full correlations for the 123 cognitive terms are reported in the **Supplementary excel**
193 **file**.

194 ***Functional connectivity: Network-based statistics (NBS)***

195 Comprehensive results/summary tables of significant regions are included in the
196 **Supplementary excel file** and results are visualized in **Fig. 3a, b**. Here, we only provide a
197 summary of the results.

198 ***Across both counting and memory control conditions.*** Notable findings include
199 widespread lower functional connectivity throughout the brain, mostly between the brainstem
200 and cortical networks, including the default-mode network (DMN), and between cortical
201 networks, such as DMN-control network [CN], and CN-salience network (SN) during EC
202 compared to both counting and memory control conditions.

203 ***EC vs counting control condition.*** We observed reduced connectivity between the
204 brainstem and somatomotor (SMN) and dorsal attention (DAN) networks (**Fig. 3a**) during EC
205 compared to the counting condition.

206 ***EC vs memory control condition.*** Interestingly, during EC, reduced functional
207 connectivity between cortical networks such as the DAN, limbic network (LN), VN, and
208 brainstem were notable (**Fig. 3b**). Additional reduced connectivity were found between the
209 cerebellum and left subcortex.

210 ***Effective connectivity: Directed network-based statistics (dNBS)***

211 Results, including excitatory and inhibitory connections, and averaged weighted in-
212 degree and out-degree are visualized in **Fig. 3c, d**. Here, we only provide a summary of the
213 results.

214 *Across both counting and memory control conditions.* No similar excitatory or
215 inhibitory connections were found across both control conditions compared to EC.

216 *EC vs counting control condition.* No notable excitatory or inhibitory connections were
217 found between EC and the counting control condition (**Fig. 3c**).

218 *EC vs memory control condition.* Both excitatory and inhibitory connections were
219 observed (**Fig. 3d**) during EC compared to the memory condition. Interestingly, inhibitory
220 connections extend to nearly all brain networks, including the subcortex and brainstem.
221 Specifically, we observed primarily excitatory connections to and from the left VN and
222 brainstem, and inhibitory connections to and from the bilateral SMN, left SN, right CN and VN.

223 *Brain reorganization: Connectivity gradients*

224 *Description and distribution of gradient values.* The principal gradient depicted in the
225 study aligns with previous research³⁰⁻³⁴, which identified a potentially hierarchical axis of
226 functional connectivity similarity variance. This axis extends from unimodal regions, primarily
227 located in the somatomotor cortex, to transmodal regions centered around the DMN and LN
228 (**Fig. 4a**). Lower principal gradient values reflect greater functional connectivity similarity to
229 unimodal cortex, whereas higher principal gradient values reflect greater functional connectivity
230 similarity to transmodal cortex. We observed a wider range of gradient distribution across all
231 networks. (**Fig. 4b**). Moreover, EC demonstrated an expansion of principal gradients compared
232 to the two control conditions (**Fig. 4c**). Results for the bootstrapped t-tests at the ROI-level are
233 presented in **Fig. 4d**, at the network-level in **Fig. 4e**. Significant results are also presented in the
234 **Supplementary excel file**. Below, we summarize the results.

235 *Across both counting and memory control conditions.* LMM at the network-level
236 revealed that EC exhibited greater gradient values in the CN. At the ROI-level, EC demonstrated
237 greater gradient values in the right frontal operculum insula, parietal cortex, and lateral PFC; and
238 lower gradient values in the bilateral visual cortex within the visual network (VN). No additional
239 significant gradient values were found.

240 *Cortical dynamics: Geometric eigenmodes*

241 *Across both counting and memory control conditions.* LMM revealed no significant
242 differences between EC and either counting or memory control conditions for mean, max, and
243 total power or energy in any eigengroups. However, LMM revealed significant differences in
244 main effects of task conditions between EC and control conditions for mean, max, or total power
245 or energy (**Fig. 5**). Specifically, EC, compared to the counting condition, had lower max ($b = -$
246 0.09 , $p = 0.006$) and total ($b = -0.14$, $p < 0.001$) power. Additionally, compared to the memory
247 control condition, EC has lower mean ($b = -0.15$, $p < 0.001$), max ($b = -0.31$, $p = 0.009$), and
248 total ($b = -0.16$, $p < 0.001$) energy, and lower mean ($b = -0.32$, $p = 0.007$), max ($b = -0.21$, $p <$
249 0.001), and total ($b = -0.37$, $p = 0.001$) power.

250 *Neurotransmitter systems receptor density: Partial least squares correlation (PLSC)*

251 PLSC extracted one significant latent variable relating neurotransmitter systems receptor
252 densities to delta-weighted-degree maps, explaining 98.85% of the covariance between the two
253 datasets ($p_{\text{spin}} = 0.023$, one-tailed). Additionally, a positive correlation was found between the
254 latent variables ($r = 0.42$, $p < 0.001$, **Fig. 6a**). We also computed the loadings for each receptor
255 (**Fig. 6b**) and delta-weighted-degree map (**Fig. 6c**), where positively loaded receptors co-vary
256 with positively loaded delta-weighted-degree in positively scored brain regions and similarly for
257 negative loadings³⁵. Projecting the neurotransmitter systems receptor density patterns back onto
258 the delta-weighted-degree weights reflects how well a brain area exhibits the receptor and delta-
259 weighted-degree weighted pattern, referred to here as ‘receptor scores’ and ‘delta-weighted-
260 degree scores’, respectively (**Fig. 6d, e**).

261 Metabotropic glutamate receptor 5 (mGluR₅), serotonin 5HT₄, and dopamine D₁
262 displayed the greatest positive loadings while histamine H₃ displayed the only negative loading
263 (**Fig. 6b**). Non-significant loadings include serotonin transporter 5HTT, mu-opioid receptor
264 MOR, norepinephrine transporter NET, and GABA_A. Both EC-Counting and EC-Memory delta
265 weighted-degree maps have similar negative loadings (**Fig. 6c**). This suggests that the
266 combination of H₃ receptor distributions co-vary with EC-related weighted-degree values in
267 unimodal regions (**Fig. 6d**). EC reduces connectivity where mGluR \square /5HT \square /D \square receptors are
268 abundant and increases connectivity where H \square receptors are abundant, relative to both control
269 tasks. Examining the brain scores, transmodal regions (PFC, PCC, temporal areas), where

270 mGluR α /5HT α /D α /NMDA receptors are rich, decrease connectivity during EC relative to both
271 controls (**Fig. 6e**). In contrast, primary sensory and motor cortices where H α receptors are
272 plenty, increase connectivity during EC. Collectively, these results demonstrate a direct link
273 between whole-brain molecular receptor distributions and EC.

274 *Neurosynth data-driven cognitive terms decoding analysis*

275 *Across both counting and memory control conditions.* Correlation analysis revealed that
276 EC was positively associated with action, attention, fixation, gaze, planning, spatial attention,
277 visual attention, and visual perception. These terms are associated with perception and planning.
278 In contrast, negative associations were found with terms such as anxiety, arousal, eating,
279 emotion, fear, loss, mood, pain, stress, and valence. These terms are associated with mental
280 suffering and psychological distress. Results are visualized in **Fig. 2**.

281 *EC vs counting control condition.* EC was additionally positively associated with
282 imagery and object recognition.

283 *EC vs memory control condition.* EC was additionally positively associated with
284 selective attention and efficiency.

285 **Discussion**

286 Using ultra-high-resolution 7T functional MRI, we present the first neural
287 characterization of an extraordinary non-conscious state of extended cessation (EC). We used an
288 intensive within-subject, dense-sampling design (N=3) , analogous to the rigorous small-N
289 primate study designs and small-N human case studies to prioritize internal validity and depth of
290 individual-level analysis^{36,37}.

291 Human consciousness is supported by integrated brain activity across functionally
292 segregated areas³⁸. Here we show that EC exhibits a distinctive reorganization of brain networks:
293 higher brain activity in unimodal brain systems (VN, DAN), and temporal pol, lower activity in
294 transmodal brain systems (DMN), as well as regions in the subcortex, brainstem, and cerebellum,
295 expansion of the principal cortical gradient, enhancing segregation between unimodal and
296 transmodal regions, and network–neurochemical coupling aligned with histaminergic H α

297 receptor topography. Furthermore, spatial meta-analytic decoding associates the EC pattern with
298 cognitive processes associated with perception/attention and reduced mental suffering and
299 psychological distress³⁹. These results suggest a reconfiguration of the limbic network^{40,41},
300 consistent with meditators' post-EC reports and enduring psychological transformation of clarity,
301 relief, and equanimity. These results offer novel insights into the neural correlates of EC,
302 highlighting its potential to influence brain function as well as ultimately our understanding of
303 consciousness and human flourishing, given the profound aftereffects reported.

304 Contrary to accounts that associate non-conscious states with global cortical
305 suppression⁴² and gradient flattening and widespread integration loss⁴³, EC showed higher local
306 activity in unimodal sensory regions and reduced activity in transmodal regions and networks,
307 specifically the DMN, and key subcortical and brainstem regions such as the caudate, thalamus,
308 globus pallidus, and ventral tegmentum area. This reduced connectivity, notably in the basal
309 ganglia⁴⁴⁻⁴⁶ and brainstem⁴⁷ could be indicative of a indicating gating of access of sensation and
310 perception⁴⁸ and wakefulness⁴⁷. These findings partially mimic patients having disorders of
311 consciousness, such as those with minimally conscious state and unresponsive wakefulness
312 syndrome⁴⁹, who also demonstrated reduced brain activity in the DMN. In contrast, the principal
313 gradient expands (unimodal values become more negative; transmodal values become more
314 positive) and the distribution was flatter across all networks in EC, suggesting specialization of
315 brain functions during EC. Unlike non-conscious states due to pharmacological interventions or
316 disorders of consciousness, EC is endogenous, volitional, and followed by equanimity rather
317 than disorientation. These contrasts support the view that multiple routes to non-conscious states
318 exist, such as pharmacologic/global suppression versus selective decoupling, with divergent
319 network consequences.

320 Two most prominent theories of consciousness are GNW and IIT. GNW posits that
321 consciousness depends on long-range recurrent broadcast across frontoparietal hubs and non-
322 consciousness accompanies reduced feedback and integration (e.g., anesthesia)²⁷. EC is partly
323 consistent with this view wherein DMN and thalamic suppression imply diminished recurrent
324 broadcast to the workspace but constrains GNW because unimodal systems (VN/DAN) remain
325 engaged and the principal gradient polarizes rather than collapses. Thus, selective decoupling of
326 recurrent access to transmodal hubs, rather than frontoparietal shutdown, can suffice to suspend

327 awareness. In contrast, IIT predicts that non-conscious states reflects reduced
328 integration/differentiation, which often manifests empirically as flattened principal gradients and
329 loss of complex spatial modes in pharmacological interventions and disorders of
330 consciousness^{28,43,50}. EC shows the opposite pattern: gradient expansion, stronger unimodal–
331 transmodal segregation in the absence of awareness, and reduced lower-order brain modes in EC.
332 This directly challenges IIT, indicating that excessive segregation rather than loss off integration
333 can also yield non-conscious states. Finally, according to AIF, loss of consciousness can arise
334 from down-weighting the precision of sensory prediction errors²⁹. Surprisingly, compared to
335 GNW and IIT, EC supports AIF on multiple fronts. The reduced activity in the thalamus and
336 brainstem together with increased activity in unimodal systems is consistent with precision
337 gating. Additionally, network–neurochemical coupling to histamine H₁ receptor topography in
338 unimodal cortex could explain neuromodulation on precision control³⁵. Finally, post-EC sensory
339 clarity and equanimity is consistent with a transient precision overshoot, a brief increase in the
340 gain assigned to sensory prediction errors which yields unusually vivid perception while self-
341 referential priors remain down-weighted. In short, EC supports precision-gating (AIF), refines
342 GNW by dissociating recurrent access from generic frontoparietal activity, and challenges IIT by
343 demonstrating non-conscious states with increased hierarchical segregation rather than uniform
344 flattening.

345 A unique contribution of this study is the link between EC and neurotransmitter receptor
346 topography. Brain activity during EC co-varies with H₁ receptors receptor topography. As
347 presynaptic autoreceptors and heteroreceptors, H₁ receptors regulate histamine release and
348 suppress acetylcholine, dopamine, and norepinephrine, shaping arousal, attention, and sensory
349 filtering⁵¹⁻⁵³. EC's coupling to H₁-dense unimodal cortices and reduced engagement of
350 transmodal hubs rich in mGluR₁/NMDA/D₁ may allow habitual cognitive constraints to relax,
351 enabling underlying intrinsic brain dynamics to emerge⁵⁴ and modulate the type of conscious
352 experience⁵⁵. This shift likely allows practitioners to re-engage perception with heightened
353 equanimity and reduced cognitive bias, providing optimal conditions for deep meditative insight.
354 Notably, similar decreases in transmodal network activity have been observed during ACAM²
355 and AIIM⁵⁶. Upon exiting EC, unimodal networks enable a rapid, equanimous re-engagement of
356 sensory processes, giving rise to the vivid clarity, equanimity, and deep insight into the
357 phenomenology of the mind practitioners describe.

358 EC may be best understood as a “reset” of consciousness, in which self-referential loops
359 are silenced, perceptual systems reorganized, and affective load attenuated. Thus, beyond the
360 field of cognitive neuroscience, EC offers a radical empirical model for advancing mental health,
361 wellbeing, and human flourishing. The transformative aftereffects of EC—including deep sense
362 of relief, clarity, equanimity, and reductions in repetitive thought, self-talk, and craving—map
363 onto diminished self-referential processing and enhanced perceptual networks, according to the
364 decoded meta-analytic cognitive maps from Neurosynth. These neural and experiential changes
365 directly address components of psychological suffering¹⁰. Finally, the neural signatures of EC
366 could serve as biomarkers for advanced meditation outcomes, guiding machine-learning-based
367 personalization of practice⁵⁷ or neuromodulation protocols to target specific meditation
368 outcomes, such as kindness, concentration, or acceptance⁵⁸. Thus, EC point towards novel
369 strategies for facilitating increasingly effective mental health interventions⁵⁹.

370 This study has considerable strengths including a whole-brain approach at high spatial
371 resolution using ultra-high-resolution fMRI data with stringent methodological approaches.
372 Nevertheless, there are several important limitations to consider. First, as this study is the first to
373 investigate extended cessation, specifically EC, our results should be considered an initial step
374 that should be replicated. While we compared EC to non-meditative states, a natural extension
375 would be to compare EC to other meditative states to elucidate similarities and differences
376 between EC and advanced forms of mediation. The absence of consciousness and self-reports
377 during EC poses a challenge in understanding the subjective non-experience and its correlation
378 with the neuroimaging findings. However, Neurosynth decoding offered robust evidence linking
379 EC brain state to enhanced perceptual clarity, sensitivity, and the absence of mental suffering.
380 These findings strongly suggest that significant brain reorganization occurs during EC to a
381 degree that supports these subjective subsequent phenomena.

382 In conclusion, our results provide the first evidence for the neural correlates of extended
383 cessation. Extended cessation is marked by higher activity in unimodal regions with
384 downregulation of transmodal and thalamic regions, expansion of cortical gradients, and reduced
385 low-order global eigenmodes. Our results supports AIF, constraints GNW, and challenges IIT.
386 These findings not only deepen our understanding of extended cessation but also illuminate
387 fundamental mechanisms underlying human consciousness. More broadly, EC reveals a selective

388 “reset” capacity of the mind that attenuates self-referential burden while sharpening perceptual
389 engagement, opening tractable neuromodulatory and behavioral routes to reduce suffering and
390 advance human flourishing.

391

392 **Materials and Methods**

393 **Participants**

394 Participants were three male advanced meditators, Subject 2 (Male, age 32 at time of data
395 collection), Subject 3 (age 46 at time of data collection), and Subject 4 (age 66 at time of data
396 collection). Important to the current study, the participants are advanced meditators and reported
397 being able to incline towards EC as the target of meditation. Subject 2 had over 19 years of
398 meditation experience with total meditation experience of an estimated at least 15,000 hours.
399 Subject 3 had over 4 years of meditation experience, and an estimated total practice amount at
400 least of 9,000 hours. Subject 4 had over 50 years of meditation experience with total meditation
401 experience of at least 35,000 hours. Lifetime practice hours are approximate self-reports based
402 on duration and frequency of weekly practice and retreats. We also note that lifetime hours are
403 not necessarily a direct measure of meditative expertise. The Mass General Brigham IRB
404 approved the study, and the participants provided informed consent.

405 **Experimental design**

406 *Extended cessation (EC)*

407 FMRI data during EC was collected as part of a larger study of advanced meditation
408 practices. In this advanced practice of EC, participants have trained extensively to develop the
409 precision to enter and exit EC at specific, predefined times. This level of mastery reflects not
410 only the ability to achieve a deep cessation state but also control over the duration and timing of
411 the state. The participants performed EC meditation as the last meditation session after all other
412 MRI sessions (structural scans, advanced concentrative absorption meditation, advanced insight
413 meditation, non-meditative control conditions) were completed. The total amount of fMRI data

414 collected for EC for each participant was approximately 45 minutes across three sessions. We
415 asked the participant to meditate, enter, and maintain EC for 15 minutes during each session.

416 An EC run started with the participant making an intention to stay in EC for only 15
417 minutes. Then the participant started meditating at the start of the EC run. As some participants
418 indicated that it was not possible for them to self-report entrance to this state, we did not attempt
419 to mark when the participant entered EC. The run ended when the participant exited out of EC
420 and indicated the exit with a button press. Retrospectively, we asked participants to estimate the
421 duration it took them to enter EC if they did not indicate with a button press initially. After
422 completing the meditation task, all participants completed a standardized EC phenomenology
423 questionnaire—designed to reflect how they typically practice and experience EC—covering
424 preparation, onset, absence of consciousness, exit, and afterglow. Two participants provided their
425 phenomenology responses after data collection had formally concluded, and their delayed reports
426 have been included in the dataset.

427 *Non-meditative control conditions*

428 We developed two non-meditative control conditions (hereon control conditions) that
429 were used to compare against EC. These control conditions were designed to engage the
430 participant's mind with non-meditative mental activities. These conditions were carefully
431 selected to be sufficiently engaging to not induce meditative states. We did not use a resting-state
432 control condition, since experienced meditators may enter meditative states during this period⁶⁰.

433 The two different control conditions implemented in this study were: (1) a memory
434 control condition in which participants were asked to reminisce the events of the past two weeks
435 and narrate them sub-vocally in their minds, closing their eyes and without moving their lips, for
436 8 minutes (min); and a (2) counting control condition, where the participants were asked to
437 mentally count down in decrements of 5 from 10,000 for 8 min, closing their eyes and without
438 moving their lips. We collected two runs for each control condition, which provided 16 mins
439 data for each control condition. However, for participant ABC, only a single run for each control
440 condition as part of another study.

441 **Neuroimaging acquisition**

442 Neuroimaging was acquired using a 7T MR scanner (SIEMENS MAGNETOM Terra)
443 using a 32-channel head coil. Functional imaging was performed using a single-shot two-
444 dimensional echo planar imaging sequence with T2*-weighted BOLD-sensitive MRI, repetition
445 time (TR) = 2.9 sec, echo time (TE) = 30 ms, flip angle (FA) = 75°, field of view (FOV) = [189 x
446 255], matrix = [172 x 232], GRAPPA factor = 3, voxel size = 1.1 x 1.1 x 1.1 mm³, 126 slices,
447 interslice distance = 0 mm, bandwidth = 1540 Hz/px, echo spacing = 0.75 ms. Slice acquisitions
448 were acquired for the whole brain, with interleaved slices, sagittal orientation, and anterior-to-
449 posterior phase encoding. Opposite phase-encoded (i.e., posterior-to-anterior) slices with the
450 same parameters were also acquired to perform distortion correction.

451 Whole-brain T1-weighted structural images were acquired as follows: TR = 2.53 sec, TE
452 = 1.65 ms, inversion time = 1.1 sec, flip angle = 7°, 0.8mm isotropic resolution, FOV = 240 x
453 240, GRAPPA factor = 2, bandwidth = 1200 Hz/Px. The participant's physiological (i.e., heart
454 rate using pulse oximetry and respiration using breathing bellows) signal recordings were
455 collected throughout the scanning session.

456 Each neuroimaging session started each time the participant's position was localized in
457 the scanner and lasted until the next localization was conducted, usually after the participant left
458 the scanner to rest, typically after two hours.

459 **Neuroimaging preprocessing**

460 Preprocessing steps were conducted at the level of MRI session and for all runs within
461 that session, similar to our previous protocol, using AFNI². Details of the preprocessing steps are
462 described in our previous study². In short, steps consisted of (1) de-spiking; (2) RETROspective
463 Image CORrection (RETROICOR)⁶¹ to regress out the effects of physiological (cardiac and
464 respiratory) noise on data; (3) slice time correction; (4) distortion correction using opposite
465 phase-encoded EPI; (5) motion correction; and (6) registering the anatomical dataset (T1) to a
466 standard (MNI152_2009) template. Additional preprocessing steps included: (7) scrubbing any
467 volume with motion > 0.3mm and had more than 5% outlier voxels; and (8) regressing out
468 eroded cerebrospinal fluid (CSF) mask time course and motion parameters (3 translations, 3
469 rotations) per run, and band-pass filtering (0.01 – 0.1Hz). Each fMRI run was then segmented

470 into one-minute segments for statistical analyses, similar to our previous work on advanced
471 meditation².

472 **Regions of interest (ROI)**

473 We used four different parcellation/segmentation schemes to define ROIs for subsequent
474 whole-brain analyses: (1) Schaefer-400 parcellation atlas for cortical areas⁶²; (2) 34-region Tian
475 subcortex atlas for subcortical regions⁶³; (3) 54 Bianciardi brainstem atlas⁶⁴; and (4) 10 Multi-
476 Domain Task Battery (MDTB) functional cerebellar atlas⁶⁵. In total our
477 parcellation/segmentation yielded 498 ROIs across the brain. For functional and effective
478 connectivity analyses specifically, we opted to use the Schaefer-100 parcellation atlas for cortical
479 areas instead of the 400 parcellation scheme⁶² and the 16-region Tian subcortex atlas for
480 subcortical regions⁶³. This decision was made to reduce the number of ROIs, thereby facilitating
481 the interpretation of whole-brain effective connectivity patterns and enabling direct
482 comparability between functional and effective connectivity results, while still maintaining a
483 reasonably high spatial resolution for cortical regions.

484 **Neuroimaging analyses**

485 *Regional homogeneity analysis*

486 Regional homogeneity (ReHo) is a measure of similarity in temporal activation pattern of
487 a voxel and its nearby voxels⁶⁶. This measure of local functional connectivity within brain
488 regions is a close derivative of underlying brain activity⁶⁶. A higher ReHo value indicates
489 stronger synchronization of local brain regions, indicating greater functional connectivity in that
490 region and thus an index of greater brain activity. In this study, we defined a cluster size of 27
491 voxels and calculated the ReHo values for each fMRI segment. We standardized the ReHo
492 values before smoothing the standardized ReHo maps using a 2 mm full-width half-maximum
493 (FWHM) kernel. The standardized ReHo values were then parcellated using the four different
494 parcellation/segmentation schemes⁶²⁻⁶⁵, yielding 498 ReHo values for each fMRI segment.

495 *Functional connectivity*

496 Data was smoothed using a 2 mm FWHM as we were interested in connectivity of
497 smaller brain regions such as the brainstem. Then for each segment, whole-brain time series of
498 the 180 brain regions as defined previously was extracted, followed by computation of 180x180
499 functional connectivity matrices using Pearson's correlation.

500 ***Effective connectivity: Regression dynamic causal modeling (rDCM)***

501 Whole-brain effective connectivity was assessed using regression dynamic causal
502 modeling (rDCM). rDCM, a variant of DCM for fMRI, enables effective connectivity analyses
503 across whole-brain networks with computational efficiency⁶⁷⁻⁷¹ without sacrificing reliability⁷².
504 The validity of this procedure has been established in both task-based and resting-state fMRI
505 studies^{67,68,70,72,73}. Specifically, rDCM incorporates modifications to DCM⁷² including: (1)
506 translation of equations into the frequency domain using Fourier transformation; (2) replacement
507 of nonlinear hemodynamic models with linear functions; (3) mean-field approximation across
508 regions; and (4) specification of priors for neuronal parameters and noise precision. These
509 modifications transform linear DCM into Bayesian linear regression in the frequency domain,
510 which ultimately facilitates highly efficient DCM model inference^{70,73}.

511 To compute effective connectivity, preprocessed data at step 6 (normalization) was first
512 smoothed using a 2 mm FWHM. Time series of each ROI were then extracted after regressing
513 out 6 motion parameters, white matter and CSF signals, with discrete cosine basis set with
514 frequency characteristics of resting-state brain dynamics (0.01– 0.1 Hz). Whole-brain effective
515 connectivity was then calculated using rDCM for resting-state fMRI⁶⁸ to examine whole-brain
516 effective connectivity^{69,74-77}. First-level rDCM models for 180 ROIs were then computed using
517 the rDCM module within the Translational Algorithms for Psychiatry Advancing Science
518 (TAPAS) toolbox⁷⁸.

519 ***Principal gradient-mapping***

520 To map the gradients, we first computed a template gradient through a multi-step process.
521 First, data was smoothed using a 6 mm FWHM kernel, followed by computation of functional
522 connectivity matrices for each segment using the Schaefer 400-regions 7-network atlas using
523 Pearson's correlation, thus producing a 400x400 functional connectivity matrix. These individual

524 matrices were then averaged across all segments, resulting in a mean functional connectivity
525 matrix. Subsequently, gradients for this mean matrix were derived by thresholding the mean
526 correlation matrix at 90% sparsity to retain only the strongest connections, followed by
527 generating a similarity matrix using cosine similarity to capture the connectivity pattern
528 similarities among ROIs. The resulting similarity matrix served as input for the diffusion map
529 embedding algorithm, from which the principal gradients were extracted. We computed a
530 template gradient from an out-of-sample dataset of 134 subjects from the HCP dataset (the
531 validation cohort used by⁷⁹).

532 Following template gradient computation, alignment with individual segment gradients
533 was performed. The principal gradient values for each fMRI segment were computed based on
534 their respective functional connectivity matrices and then aligned with the template gradient
535 using Procrustes rotations with 10 iterations to ensure optimal comparison across datasets. All
536 analyses described herein were conducted using the BrainSpace toolbox implemented in
537 Python⁷⁹. Using the gradient values obtained from gradient alignment, we computed the average
538 network gradient values for each network by averaging the gradient values of all the parcels
539 within that network.

540 *Cortical dynamics: Geometric eigenmodes*

541 To decompose fMRI activity into 200 frequency-specific eigenmodes, we used geometric
542 eigenmodes derived from a population-averaged midsurface thickness template of the neocortical
543 surface from Pang et al., wherein the methods to generate these geometric eigenmode templates
544 are also described⁸⁰. Briefly, the geometric eigenmodes were computed by constructing the
545 Laplace-Beltrami operator from the cortical mesh and solving the eigenvalue problem. The
546 resulting eigenvalues are ordered according to spatial frequency/wavelength of each mode,
547 where mode 1 has the longest wavelength (lowest frequency) while higher modes have shorter
548 wavelengths (higher frequency). Conversely, eigenmodes are the complete basis set—a weighted
549 sum of varying-wavelength modes. Lower-numbered modes capture large-scale spatial patterns
550 (e.g. left/right hemisphere, anterior/posterior regions) while higher-number modes correspond to
551 smaller-scale spatial patterns where functional properties of nearby regions vary independent of
552 proximity.

553 Using the geometric eigenmodes, we decomposed functional MRI data to reveal
554 emerging cortical spatiotemporal dynamic patterns by examining the contribution of each
555 eigenmode to the cortical activity at each time instance. At each time point of each fMRI time
556 courses, fMRI data were projected onto each of the 200 geometric eigenmodes, yielding the
557 temporal activity of the particular eigenmode in a method described previously^{81,82}.
558 Subsequently, the temporal activation of eigenmodes were analyzed in terms of their power (the
559 strength of an eigenmode's activation at a given fMRI time instance: $|\omega_k(t_i)|$) and energy (the
560 eigenmode's frequency-weighted contribution, estimated by weighting the square of the
561 eigenmode's strength of activation by the square of its corresponding eigenvalue (λ_k) at each time
562 point: $|\omega_k(t_i)|^2 \lambda_k^2$) at each fMRI time point. Mean power and energy were calculated by averaging
563 the power and energy of each eigenmode across all time points in a single segment (i.e. yielding
564 200 mean power and energy values for 200 modes per fMRI segment). Maximum power and
565 energy were calculated as the maximum spectra value for a given eigenmode across all time
566 points within a segment (i.e. yielding 200 maximum power and energy values for 200 modes per
567 fMRI segment). Unless otherwise noted, all reported maximum and mean power and energy
568 values are reported on a log-scale⁸². Brain total power and total energy were computed by
569 summing power and energy across all eigenmodes for each time point and then averaging all
570 time points within a segment.

571 ***Influence of neurotransmitter systems receptor density: Positron Emission Tomography (PET)***
572 ***neurotransmitter systems receptor density maps***

573 We used a recently made available public neurotransmitter systems receptor density maps
574 for 19 receptors and transporters, across 9 neurotransmitter systems by Hansen and colleagues
575 at https://github.com/netneurolab/hansen_receptors³⁵. These include dopamine (D₁, D₂, DAT)
576 noradrenaline (NAT), serotonin(5-HT_{1A}, 5-HT_{1B}, 5-HT_{2A}, 5-HT₄, 5-HT₆, 5-HTT), acetylcholine
577 ($\alpha_4\beta_2$, M₁, VACHT), glutamate (mGluR₅, NMDA), GABA (GABA_A), histamine (H₃),
578 cannabinoid (CB₁), and opioid (MOR) receptors. Details regarding the neurotransmitter systems
579 receptor density maps, each PET dataset, and their respective acquisition and limitations can be
580 found in ref³⁵. Volumetric PET images were registered to the MNI-ICBM 152 nonlinear 2009
581 (version c, asymmetric) template, averaged across participants within each study, and then

582 parcellated and receptors/transporters with more than one mean image of the same tracer were
583 combined using a weighted average³⁵.

584 *Decoding of brain activity using data-driven Neurosynth cognitive maps*

585 To provide a complementary approach for analyzing brain activity patterns with behavior
586 in the absence of behavioral data, we examined the spatial similarity of ReHo maps with 123
587 meta-analytic brain maps derived from the Neurosynth database. Neurosynth generates
588 probabilistic measurements that can be interpreted as a quantitative representation of the
589 association between regional fluctuations in activity and psychological processes. Although
590 Neurosynth's database contains over 1,000 terms, we narrowed our focus to terms related to
591 cognition and behavior, drawing from previous research^{35,83,84}. Our selected set of 123 terms
592 encompasses broad categories, ranging from attention and emotion, to more specific processes
593 such as visual attention and episodic memory. The terms also include basic behaviors (e.g.,
594 eating and sleep) and emotional states (e.g., fear and anxiety).

595 **Statistical analysis**

596 *ReHo brain activity*

597 Linear mixed-effects models were used to analyze ReHo differences between EC and
598 control conditions. The model included task condition as a fixed effect and random intercepts for
599 participant and for segments nested within subject. Corrections for multiple comparisons across
600 models were applied using false-discovery rate (FDR) across all 498 ROIs. We used Dunnett's
601 test to compare the difference between EC and control tasks, with EC as the reference group
602 controlling for multiple comparisons using Bonferroni correction for $k = 2$ comparisons. For ease
603 of interpretation, all coefficients were flipped to retrieve the contrast of EC against the control
604 conditions. Analyses were conducted in R⁸⁵ loading on R Studio v2022.12.0.353.20⁸⁶.

605 *Functional connectivity: Network-based statistics (NBS)*

606 NBS was used to explore functional connectivity differences between EC and control
607 conditions in the whole-brain network containing 198 nodes and $19,503 \left(\frac{198 \times 197}{2}\right)$ unique edges⁸⁷.
608 NBS is a nonparametric statistical method used to perform mass-univariate statistical tests for

609 multiple graph comparisons. NBS identifies interconnected subnetworks exhibiting significant
610 differences in functional connectivity between groups or conditions. Instead of treating
611 connections independently, NBS leverages the inherent interconnectedness of the brain by
612 identifying clusters of connections collectively differing across groups. This enables sensitive
613 detection of subtle yet interconnected alterations in whole-brain functional connectivity. T-scores
614 were computed for each pairwise connection under contrasts EC > control and EC < control
615 separately, with additional separate analyses for counting and memory control conditions. Each
616 test was conducted at the primary threshold ($t = 3.1$, $p = 0.025$) to select the suprathreshold
617 connections for which the t-scores exceeded the primary t-value. We used $p = 0.025$ to
618 accommodate two contrasts per control comparison (EC > control and EC < control). Connected
619 components where the EC showed higher or lower functional connectivity than the control
620 conditions were identified, and the number of the edges or their size was stored. A permutation
621 test was then performed to determine the significance of each component by comparing its size
622 to the distribution of maximum component sizes under random group assignments (5000
623 permutations). Corrected p-values were computed as the proportion of permutations with larger
624 maximum components than the observed size. NBS enabled sensitive detection of interconnected
625 functional connectivity alterations in EC by leveraging the inherent network structure of the
626 brain and rigorously accounting for multiple comparisons.

627 *Effective connectivity: Directed network-based statistics (dNBS)*

628 dNBS, an extension of NBS, was used to analyze effective connectivity differences
629 between EC and control conditions. We investigated two contrast, EC > control and EC < control
630 separately, with additional separate analyses for counting and memory control conditions. The
631 statistical significance of the outcomes was determined using a primary threshold of $t = 3.1$ ($p =$
632 0.025) and 5000 permutations, following the same procedures as in the conventional NBS
633 approach. The key distinction between dNBS and NBS lies in the fact that dNBS analyzes twice
634 the number of edges compared to NBS, accommodating the directional nature of effective
635 connectivity measures.

636 *Brain organization: Connectivity gradients*

637 Linear mixed-effects models were used to analyze cortical principal gradient differences
638 between EC and control conditions. These tests were performed at both the network-level,
639 encompassing 7 cortical networks, and at the ROI-level, comprising 400 ROIs. This dual
640 approach allowed for a robust examination of gradient variations across different scales of
641 cortical organization. Corrections for multiple comparisons were applied using false-discovery
642 rate across the 7 networks and 400 ROIs respectively.

643 ***Cortical dynamics of EC: Geometric eigenmode power and energy***

644 To analyze differences in frequency-specific eigenmode mean power and energy between
645 EC and control conditions while minimizing multiple comparisons, we utilized 15 eigengroups:
646 grouping of eigenmodes according to spatial frequency^{80,88}. Eigengroups provide a way to
647 aggregate degenerate solutions from the solving of the eigendecomposition such that eigenmodes
648 with the same number of nodal lines and wavelengths are grouped together. This method allows
649 for investigation of eigenmode metrics that are less affected by noise^{89,90}. Using this approach,
650 each eigengroup's power and energy were then compared as reference values to both counting
651 and memory control conditions using linear mixed-effects models. The resulting *p*-values were
652 FDR corrected across both control condition comparisons. Finally, linear regression was used to
653 examine mean power and energy differences between EC and control conditions.

654 ***Influence of neurotransmitter systems receptor density: Partial least squares correlation***

655 We used partial least squares correlation (PLSC) analysis to explore the multivariate
656 relationship between neurotransmitter systems receptor densities and EC delta-weighted-degree
657 connectivity maps. PLSC is an unsupervised multivariate statistical technique that decomposes
658 two datasets into orthogonal sets of latent variables with the goal of maximizing covariance
659 between them⁹¹. In this context, the latent variables consist of receptor weights, EC-control
660 weighted-degree weights and a singular value that represents the covariance between receptor
661 distributions and weighted-degree connectivity that is explained by the latent variable.

662 EC delta-weighted-degree maps were created by first thresholding all negative-weighted
663 connectivity and self-connections to zero, followed by summing each region's positive
664 connection weights to all other regions. we only use cortical atlas for this analysis, similar to

665 previous research on chemoarchitecture of the brain^{35,83}. Segment-level weighted-degree vectors
666 were then averaged across all segments within each task, producing a single weighted-degree
667 profile per participant per task. For each participant, the delta-weighted-degree map was
668 calculated as the difference between EC and each control task, i.e., EC-Counting, and EC-
669 memory. Finally, participant-level delta-weighted-degree profiles were then averaged across the
670 three participants to obtain the two delta-weighted-degree maps, EC-Counting, and EC-memory.

671 By projecting the original receptor density and weighted-degree data onto the
672 corresponding latent variable weights, we computed receptor and EC-difference scores,
673 assigning each brain region a specific score for both. Receptor loadings were then calculated as
674 the Pearson correlation between neurotransmitter systems receptor densities and receptor scores,
675 with a similar process used to compute EC-difference loadings (weighted-degree map and EC-
676 difference scores). Importantly, PLSC does not (1) infer causal links between receptors and EC,
677 (2) establish univariate associations between specific receptors and EC, or (3) rule out the
678 possibility of additional connections between receptors and EC.

679 We assessed the significance of each latent variable's singular value using permutation
680 spin-testing⁹²⁻⁹⁴. For each map, parcel coordinates were projected onto the spherical surface and
681 then randomly rotated and original parcels were reassigned the value of the closest rotated parcel
682 (10,000 repetitions)⁹⁵. In addition to preserving the distribution of cortical values, this null model
683 also preserves the spatial autocorrelation present in the data.

684 ***Contextualization of brain activity with Neurosynth cognitive maps***

685 We used the *continuous.CorrelationDecoder* function from the NiMARE python package
686 to contextualization of brain activity with Neurosynth cognitive maps⁹⁶. We first fetched
687 Neurosynth dataset and converted it to NiMARE dataset. Following, we retrieved the 123
688 cognitive terms from the database. We also computed delta-ReHo maps (EC-counting, and EC-
689 memory) for decoding. Finally, we used the *CorrelationDecoder* function to decode the
690 association between the unthresholded delta-ReHo maps and cognitive maps.

691

692

693 References

- 694 1 Seth, A. K. & Bayne, T. Theories of consciousness. *Nat Rev Neurosci* **23**, 439-452 (2022).
695 <https://doi.org/10.1038/s41583-022-00587-4>
- 696 2 Yang, W. F. Z. *et al.* Intensive whole-brain 7T MRI case study of volitional control of
697 brain activity in deep absorptive meditation states. *Cerebral Cortex* **34**, bhad408 (2024).
- 698 3 Chowdhury, A. *et al.* Multimodal neurophenomenology of advanced concentration
699 absorption meditation: An intensively sampled case study of Jhana. *Neuroimage* **305**,
700 120973 (2025).
- 701 4 Chowdhury, A. *et al.* Investigation of advanced mindfulness meditation "cessation"
702 experiences using EEG spectral analysis in an intensively sampled case study.
703 *Neuropsychologia* **190**, 108694 (2023).
- 704 5 van Lutterveld, R., Cahaly, T., Ingram, D. & Sacchet, M. D. Brain criticality and
705 advanced meditation "cessation" events: An intensively sampled electroencephalography
706 case study. *SSRN* (2025). <https://doi.org/10.2139/ssrn.5296987>
- 707 6 Berkovich-Ohana, A. A case study of a meditation-induced altered state: increased
708 overall gamma synchronization. *Phenomenology and the Cognitive Sciences* **16**, 91-106
709 (2015).
- 710 7 van Lutterveld, R., Chowdhury, A., Ingram, D. M. & Sacchet, M. D.
711 Neurophenomenological Investigation of Mindfulness Meditation "Cessation"
712 Experiences Using EEG Network Analysis in an Intensively Sampled Adept Meditator.
713 *Brain Topogr* (2024).
- 714 8 Laukkonen, R. E. *et al.* Cessations of consciousness in meditation: Advancing a scientific
715 understanding of nirodha samāpatti. *Progress in Brain Research* **280**, 61-87 (2023).
- 716 9 Sacchet, M. D., Fava, M. & Garland, E. L. Modulating self-referential processing through
717 meditation and psychedelics: Is scientific investigation of self-transcendence clinically
718 relevant? *World Psychiatry* **23**, 298-299 (2024).
- 719 10 Sparby, T. & Sacchet, M. D. The Third Wave of Meditation and Mindfulness Research
720 and Implications for Challenging Experiences: Negative Effects, Transformative
721 Psychological Growth, and Forms of Happiness. *Mindfulness* (2025).
722 <https://doi.org/10.1007/s12671-025-02607-7>
- 723 11 Wright, M. J., Sanguinetti, J. L., Young, S. & Sacchet, M. D. Uniting contemplative
724 theory and scientific investigation: Toward a comprehensive model of the mind.
725 *Mindfulness* **14**, 1088–1101 (2023).
- 726 12 Galante, J. *et al.* A framework for the empirical investigation of mindfulness meditative
727 development. *Mindfulness* **14**, 1054–1067 (2023).
- 728 13 Amaro, A. Realization Is Here and Now. *Mindfulness* **12**, 795-797 (2020).
729 <https://doi.org/10.1007/s12671-020-01526-z>
- 730 14 Anālayo, B. The Four Levels of Awakening. *Mindfulness* **12**, 831-840 (2020).
731 <https://doi.org/10.1007/s12671-020-01530-3>
- 732 15 Rose, K. *Yoga, Meditation, and Mysticism: Contemplative Universals and Meditative*
733 *Landmarks*. (Bloomsbury Academic, 2016).
- 734 16 Toan, L. N. Salvation, Enlightenment and Awakening in Shaping Followers' Perception
735 and Understanding of Their Faith: A Linguistic Exploration. *International Journal of*
736 *Religion* **5**, 286-299 (2024). <https://doi.org/10.61707/mvedkv66>

- 737 17 Sandilands, O. & Ingram, D. M. Documenting and defining emergent phenomenology:
738 theoretical foundations for an extensive research strategy. *Front Psychol* **15**, 1340335
739 (2024). <https://doi.org/10.3389/fpsyg.2024.1340335>
- 740 18 Wright, M. J., Cha, V. L., Streifert, M. R., Ingram, D. M. & Sacchet, M. D. Risk Factors
741 for Emergence of Sudden Unusual Mental or Somatic Experiences and Subsequent
742 Suffering. *Clinical Psychological Science* (2025).
- 743 19 Wright, M. J. *et al.* Altered States of Consciousness are Prevalent and Insufficiently
744 Supported Clinically: A Population Survey. *Mindfulness* **15**, 1162-1175 (2024).
745 <https://doi.org/10.1007/s12671-024-02356-z>
- 746 20 Pujol, J. *et al.* Largest scale dissociation of brain activity at propofol-induced loss of
747 consciousness. *Sleep* **44** (2021). <https://doi.org/10.1093/sleep/zsaa152>
- 748 21 Pujol, J. *et al.* Mapping the neural systems driving breathing at the transition to
749 unconsciousness. *Neuroimage* **246**, 118779 (2022).
750 <https://doi.org/10.1016/j.neuroimage.2021.118779>
- 751 22 Noriaki, H. Nirodhasamapatti-Its Historical Meaning in the Vijñaptimatratra System.
752 *Indogaku Bukkyōgaku kenkyū* **23**, 1084-1074 (n.d.).
- 753 23 Gunaratana, M. H. *The Path of Serenity and Insight*. (Motilal Banarsidass, 1985).
- 754 24 Nanamoli, B. & Bodhi, B. *The Middle Length Discourses of the Buddha: A Translation*
755 *of the Majjhima Nikāya*. (Wisdom Publications, 2009).
- 756 25 Griffiths, P. J. *On being mindless : Buddhist meditation and the mind-body problem*.
757 (Open Court, 1986).
- 758 26 Lusthaus, D. *Buddhist Phenomenology : a Philosophical Investigation of Yogacara*
759 *Buddhism and the Ch'eng Wei-shih Lun*. (RoutledgeCurzon, 2002).
- 760 27 Mashour, G. A., Roelfsema, P., Changeux, J. P. & Dehaene, S. Conscious Processing and
761 the Global Neuronal Workspace Hypothesis. *Neuron* **105**, 776-798 (2020).
762 <https://doi.org/10.1016/j.neuron.2020.01.026>
- 763 28 Tononi, G., Boly, M., Massimini, M. & Koch, C. Integrated information theory: from
764 consciousness to its physical substrate. *Nat Rev Neurosci* **17**, 450-461 (2016).
765 <https://doi.org/10.1038/nrn.2016.44>
- 766 29 Parr, T., Pezzulo, G. & Friston, K. J. *Active Inference: The Free Energy Principle in*
767 *Mind, Brain, and Behavior*. (The MIT Press, 2022).
- 768 30 Girn, M. *et al.* Serotonergic psychedelic drugs LSD and psilocybin reduce the
769 hierarchical differentiation of unimodal and transmodal cortex. *Neuroimage* **256**, 119220
770 (2022).
- 771 31 Margulies, D. S. *et al.* Situating the default-mode network along a principal gradient of
772 macroscale cortical organization. *Proc Natl Acad Sci U S A* **113**, 12574-12579 (2016).
- 773 32 Timmermann, C. *et al.* Human brain effects of DMT assessed via EEG-fMRI. *Proc Natl*
774 *Acad Sci U S A* **120**, e2218949120 (2023). <https://doi.org/10.1073/pnas.2218949120>
- 775 33 Zhang, H. *et al.* Cortical connectivity gradients and local timescales during cognitive
776 states are modulated by cognitive loads. *Brain Struct Funct* **227**, 2701-2712 (2022).
777 <https://doi.org/10.1007/s00429-022-02564-0>
- 778 34 Zhang, J. *et al.* Intrinsic Functional Connectivity is Organized as Three Interdependent
779 Gradients. *Sci Rep* **9**, 15976 (2019). <https://doi.org/10.1038/s41598-019-51793-7>
- 780 35 Hansen, J. Y. *et al.* Mapping neurotransmitter systems to the structural and functional
781 organization of the human neocortex. *Nat Neurosci* **25**, 1569-1581 (2022).
782 <https://doi.org/10.1038/s41593-022-01186-3>

- 783 36 Becker, A. The benefits of single-subject research designs and multi-methodological
784 approaches for neuroscience research. *Front Hum Neurosci* **17**, 1190412 (2023).
785 <https://doi.org/10.3389/fnhum.2023.1190412>
- 786 37 Milne, A. E., Petkov, C. I. & Wilson, B. Auditory and Visual Sequence Learning in
787 Humans and Monkeys using an Artificial Grammar Learning Paradigm. *Neuroscience*
788 **389**, 104-117 (2018). <https://doi.org/10.1016/j.neuroscience.2017.06.059>
- 789 38 Alkire, M. T., Hudetz, A. G. & Tononi, G. Consciousness and anesthesia. *Science* **322**,
790 876-880 (2008).
- 791 39 Yang, W. F. Z., Chowdhury, A., Sparby, T. & Sacchet, M. D. Deconstructing the self and
792 reshaping perceptions: An intensive whole-brain 7T MRI case study of the stages of
793 insight during advanced investigative insight meditation. *NeuroImage*, 120968 (In press).
- 794 40 Herlin, B., Navarro, V. & Dupont, S. The temporal pole: From anatomy to function-A
795 literature appraisal. *J Chem Neuroanat* **113**, 101925 (2021).
796 <https://doi.org/10.1016/j.jchemneu.2021.101925>
- 797 41 Ralph, M. A., Jefferies, E., Patterson, K. & Rogers, T. T. The neural and computational
798 bases of semantic cognition. *Nat Rev Neurosci* **18**, 42-55 (2017).
799 <https://doi.org/10.1038/nrn.2016.150>
- 800 42 Tanabe, S. *et al.* Altered Global Brain Signal during Physiologic, Pharmacologic, and
801 Pathologic States of Unconsciousness in Humans and Rats. *Anesthesiology* **132**, 1392-
802 1406 (2020). <https://doi.org/10.1097/ALN.0000000000003197>
- 803 43 Huang, Z., Mashour, G. A. & Hudetz, A. G. Functional geometry of the cortex encodes
804 dimensions of consciousness. *Nat Commun* **14**, 72 (2023).
805 <https://doi.org/10.1038/s41467-022-35764-7>
- 806 44 Seo, J., Kim, D. J., Choi, S. H., Kim, H. & Min, B. K. The thalamocortical inhibitory
807 network controls human conscious perception. *Neuroimage* **264**, 119748 (2022).
808 <https://doi.org/10.1016/j.neuroimage.2022.119748>
- 809 45 Wolff, M., Morceau, S., Folkard, R., Martin-Cortecero, J. & Groh, A. A thalamic bridge
810 from sensory perception to cognition. *Neuroscience and Biobehavioral Reviews* **120**,
811 222-235 (2021). <https://doi.org/10.1016/j.neubiorev.2020.11.013>
- 812 46 Redinbaugh, M. J. & Saalman, Y. B. Contributions of basal ganglia circuits to
813 perception, attention, and consciousness. *Journal of Cognitive Neuroscience* **36**, 1620-
814 1642 (2024).
- 815 47 Edlow, B. L. *et al.* Multimodal MRI reveals brainstem connections that sustain
816 wakefulness in human consciousness. *Science Translational Medicine* **16**, eadj4303
817 (2024).
- 818 48 Redinbaugh, M. J. & Saalman, Y. B. Contributions of Basal Ganglia Circuits to
819 Perception, Attention, and Consciousness. *Journal of Cognitive Neuroscience* **36**, 1620-
820 1642 (2024). https://doi.org/10.1162/jocn_a_02177pathways
- 821 49 Wang, Y. *et al.* Regional Homogeneity Alterations in Patients with Impaired
822 Consciousness. An Observational Resting-State fMRI Study. *Neuroradiology* **64**, 1391-
823 1399 (2022). <https://doi.org/10.1007/s00234-022-02911-2>
- 824 50 Luppi, A. I. *et al.* Distributed harmonic patterns of structure-function dependence
825 orchestrate human consciousness. *Commun Biol* **6**, 117 (2023).
- 826 51 Lin, J. S., Sergeeva, O. A. & Haas, H. L. Histamine H3 receptors and sleep-wake
827 regulation. *J Pharmacol Exp Ther* **336**, 17-23 (2011).
828 <https://doi.org/10.1124/jpet.110.170134>

- 829 52 Yu, X., Franks, N. P. & Wisden, W. Sleep and Sedative States Induced by Targeting the
830 Histamine and Noradrenergic Systems. *Front Neural Circuits* **12**, 4 (2018).
831 <https://doi.org/10.3389/fncir.2018.00004>
- 832 53 Esbenshade, T. A. *et al.* The histamine H3 receptor: an attractive target for the treatment
833 of cognitive disorders. *Br J Pharmacol* **154**, 1166-1181 (2008).
834 <https://doi.org/10.1038/bjp.2008.147>
- 835 54 Tal, H., Wright, M., Prest, S., Sandved-Smith, L. & Sacchet, M. D. Active inference,
836 computational phenomenology, and advanced meditation: Toward the formalization of
837 the experience of meditation. *PsyArXiv* (2025). https://doi.org/10.31234/osf.io/pm5y2_v2
- 838 55 Zilles, K., Bacha-Trams, M., Palomero-Gallagher, N., Amunts, K. & Friederici, A. D.
839 Common molecular basis of the sentence comprehension network revealed by
840 neurotransmitter receptor fingerprints. *Cortex* **63**, 79-89 (2015).
841 <https://doi.org/10.1016/j.cortex.2014.07.007>
- 842 56 Yang, W. F. Z., Chowdhury, A., Sparby, T. & Sacchet, M. D. Deconstructing the self and
843 reshaping perceptions: An intensive whole-brain 7T MRI case study of the stages of
844 insight during advanced investigative insight meditation. *Neuroimage* **305**, 120968
845 (2025).
- 846 57 Guidotti, R. *et al.* Long-Term and Meditation-Specific Modulations of Brain
847 Connectivity Revealed Through Multivariate Pattern Analysis. *Brain Topogr* **36**, 409-418
848 (2023). <https://doi.org/10.1007/s10548-023-00950-3>
- 849 58 Sezer, I., Pizzagalli, D. A. & Sacchet, M. D. Resting-state fMRI functional connectivity
850 and mindfulness in clinical and non-clinical contexts: A review and synthesis.
851 *Neuroscience and Biobehavioral Reviews* **135**, 104583 (2022).
- 852 59 Abellaneda-Perez, K., Potash, R. M., Pascual-Leone, A. & Sacchet, M. D.
853 Neuromodulation and meditation: A review and synthesis toward promoting well-being
854 and understanding consciousness and brain. *Neurosci Biobehav Rev* **166**, 105862 (2024).
855 <https://doi.org/10.1016/j.neubiorev.2024.105862>
- 856 60 Tang, Y. Y., Rothbart, M. K. & Posner, M. I. Neural correlates of establishing,
857 maintaining, and switching brain states. *Trends in Cognitive Sciences* **16**, 330-337 (2012).
- 858 61 Glover, G. H., Li, T. Q. & Ress, D. Image-based method for retrospective correction of
859 physiological motion effects in fMRI: RETROICOR. *Magnetic Resonance in Medicine*
860 **44**, 162-167 (2000).
- 861 62 Schaefer, A. *et al.* Local-Global Parcellation of the Human Cerebral Cortex from
862 Intrinsic Functional Connectivity MRI. *Cerebral Cortex* **28**, 3095-3114 (2018).
- 863 63 Tian, Y., Margulies, D. S., Breakspear, M. & Zalesky, A. Topographic organization of
864 the human subcortex unveiled with functional connectivity gradients. *Nature*
865 *Neuroscience* **23**, 1421-1432 (2020).
- 866 64 Bianciardi, M. *et al.* In vivo functional connectome of human brainstem nuclei of the
867 ascending arousal, autonomic, and motor systems by high spatial resolution 7-Tesla fMRI.
868 *MAGMA* **29**, 451-462 (2016).
- 869 65 King, M., Hernandez-Castillo, C. R., Poldrack, R. A., Ivry, R. B. & Diedrichsen, J.
870 Functional boundaries in the human cerebellum revealed by a multi-domain task battery.
871 *Nature Neuroscience* **22**, 1371-1378 (2019).
- 872 66 Zang, Y., Jiang, T., Lu, Y., He, Y. & Tian, L. Regional homogeneity approach to fMRI
873 data analysis. *Neuroimage* **22**, 394-400 (2004).

- 874 67 Frassle, S. *et al.* A generative model of whole-brain effective connectivity. *Neuroimage*
875 **179**, 505-529 (2018). <https://doi.org/10.1016/j.neuroimage.2018.05.058>
- 876 68 Frassle, S. *et al.* Regression DCM for fMRI. *Neuroimage* **155**, 406-421 (2017).
- 877 69 Friston, K. J., Harrison, L. & Penny, W. Dynamic causal modelling. *Neuroimage* **19**,
878 1273-1302 (2003).
- 879 70 Frassle, S. *et al.* Whole-brain estimates of directed connectivity for human connectomics.
880 *Neuroimage* **225**, 117491 (2021).
- 881 71 Razi, A. *et al.* Large-scale DCMs for resting-state fMRI. *Network Neuroscience* **1**, 222-
882 241 (2017).
- 883 72 Frassle, S. & Stephan, K. E. Test-retest reliability of regression dynamic causal modeling.
884 *Netw Neurosci* **6**, 135-160 (2022).
- 885 73 Frassle, S. *et al.* Regression dynamic causal modeling for resting-state fMRI. *Hum Brain*
886 *Mapp* **42**, 2159-2180 (2021). <https://doi.org/10.1002/hbm.25357>
- 887 74 Friston, K. J. Functional and effective connectivity: a review. *Brain Connect* **1**, 13-36
888 (2011).
- 889 75 Friston, K. J., Kahan, J., Biswal, B. & Razi, A. A DCM for resting state fMRI.
890 *Neuroimage* **94**, 396-407 (2014).
- 891 76 Friston, K. J. *et al.* Bayesian model reduction and empirical Bayes for group (DCM)
892 studies. *Neuroimage* **128**, 413-431 (2016).
- 893 77 Razi, A., Kahan, J., Rees, G. & Friston, K. J. Construct validation of a DCM for resting
894 state fMRI. *Neuroimage* **106**, 1-14 (2015).
- 895 78 Frassle, S. *et al.* TAPAS: An Open-Source Software Package for Translational
896 Neuromodeling and Computational Psychiatry. *Front Psychiatry* **12**, 680811 (2021).
897 <https://doi.org/10.3389/fpsy.2021.680811>
- 898 79 Vos de Wael, R. *et al.* BrainSpace: a toolbox for the analysis of macroscale gradients in
899 neuroimaging and connectomics datasets. *Commun Biol* **3**, 103 (2020).
900 <https://doi.org/10.1038/s42003-020-0794-7>
- 901 80 Pang, J. C. *et al.* Geometric constraints on human brain function. *Nature* **618**, 566-574
902 (2023). <https://doi.org/10.1038/s41586-023-06098-1>
- 903 81 Atasoy, S., Donnelly, I. & Pearson, J. Human brain networks function in connectome-
904 specific harmonic waves. *Nature Communications* **7**, 10340 (2016).
- 905 82 Atasoy, S. *et al.* Connectome-harmonic decomposition of human brain activity reveals
906 dynamical repertoire re-organization under LSD. *Scientific Reports* **7**, 17661 (2017).
- 907 83 Luppi, A. I. *et al.* In vivo mapping of pharmacologically induced functional
908 reorganization onto the human brain's neurotransmitter landscape. *Science Advances* **9**,
909 eadf8332 (2023). <https://doi.org/doi:10.1126/sciadv.adf8332>
- 910 84 Yarkoni, T., Poldrack, R. A., Nichols, T. E., Van Essen, D. C. & Wager, T. D. Large-
911 scale automated synthesis of human functional neuroimaging data. *Nature Methods* **8**,
912 665-670 (2011). <https://doi.org/10.1038/nmeth.1635>
- 913 85 R: A Language and Environment for Statistical Computing (R Foundation for Statistical
914 Computing, Vienna, Austria, 2022).
- 915 86 RStudio: Integrated Development Environment for R (Posit Software, PBC
916 <http://www.posit.co>, Boston, MA, 2022).
- 917 87 Zalesky, A., Fornito, A. & Bullmore, E. T. Network-based statistic: identifying
918 differences in brain networks. *Neuroimage* **53**, 1197-1207 (2010).
919 <https://doi.org/10.1016/j.neuroimage.2010.06.041>

- 920 88 Chen, Y.-C. *et al.* The individuality of shape asymmetries of the human cerebral cortex.
921 *eLife* **11**, e75056 (2022). <https://doi.org/10.7554/eLife.75056>
- 922 89 Cao, T. *et al.* Mode-based morphometry: A multiscale approach to mapping human
923 neuroanatomy. *Human Brain Mapping* **45**, e26640 (2024).
924 <https://doi.org/10.1002/hbm.26640>
- 925 90 Boyes, A. *et al.* Geometric eigenmode brain fingerprinting and its longitudinal
926 associations with adolescent mental health and wellbeing. *bioRxiv*,
927 2024.2008.2008.607260 (2024). <https://doi.org/10.1101/2024.08.08.607260>
- 928 91 Krishnan, A., Williams, L. J., McIntosh, A. R. & Abdi, H. Partial Least Squares (PLS)
929 methods for neuroimaging: a tutorial and review. *Neuroimage* **56**, 455-475 (2011).
930 <https://doi.org/10.1016/j.neuroimage.2010.07.034>
- 931 92 Alexander-Bloch, A. F. *et al.* On testing for spatial correspondence between maps of
932 human brain structure and function. *Neuroimage* **178**, 540-551 (2018).
933 <https://doi.org/10.1016/j.neuroimage.2018.05.070>
- 934 93 Markello, R. D. & Misic, B. Comparing spatial null models for brain maps. *Neuroimage*
935 **236**, 118052 (2021). <https://doi.org/10.1016/j.neuroimage.2021.118052>
- 936 94 Vasa, F. & Misic, B. Null models in network neuroscience. *Nat Rev Neurosci* **23**, 493-
937 504 (2022). <https://doi.org/10.1038/s41583-022-00601-9>
- 938 95 Vazquez-Rodriguez, B. *et al.* Gradients of structure-function tethering across neocortex.
939 *Proc Natl Acad Sci U S A* **116**, 21219-21227 (2019).
940 <https://doi.org/10.1073/pnas.1903403116>
- 941 96 Salo, T. *et al.* NiMARE: neuroimaging meta-analysis research environment. *Aperture*
942 *Neuro* **3**, 1-32 (2023). <https://doi.org/10.52294/001c.87681>
- 943
- 944
- 945

946 **Author contributions**

947 Conceptualization: MDS; Funding Acquisition: MDS; Methodology: MDS, TS; Data Collection:
948 MDS, TS, RP, WFZY; Software: WFZY, GM, IB, RP; Formal Analysis: WFZY, AK, KA, GM,
949 IB; Writing – Original Draft: WFZY and MDS; Writing – Review & Editing: WFZY, MDS, AK,
950 KA, RP, and TS.

951

952 **Funding information**

953 Dr. Sacchet and the Meditation Research Program are supported by the Dimension Giving Fund,
954 Tan Teo Charitable Foundation, and additional individual donors. Dr. Abellaneda-Pérez was
955 financially supported by a Juan de la Cierva research grant (FJC2021-047380-I) of the Spanish
956 Ministry of Science and Innovation. Dr. Terje Sparby is supported by Software AG Stiftung.

957

958 **Competing interests**

959 All authors declare no competing interests.

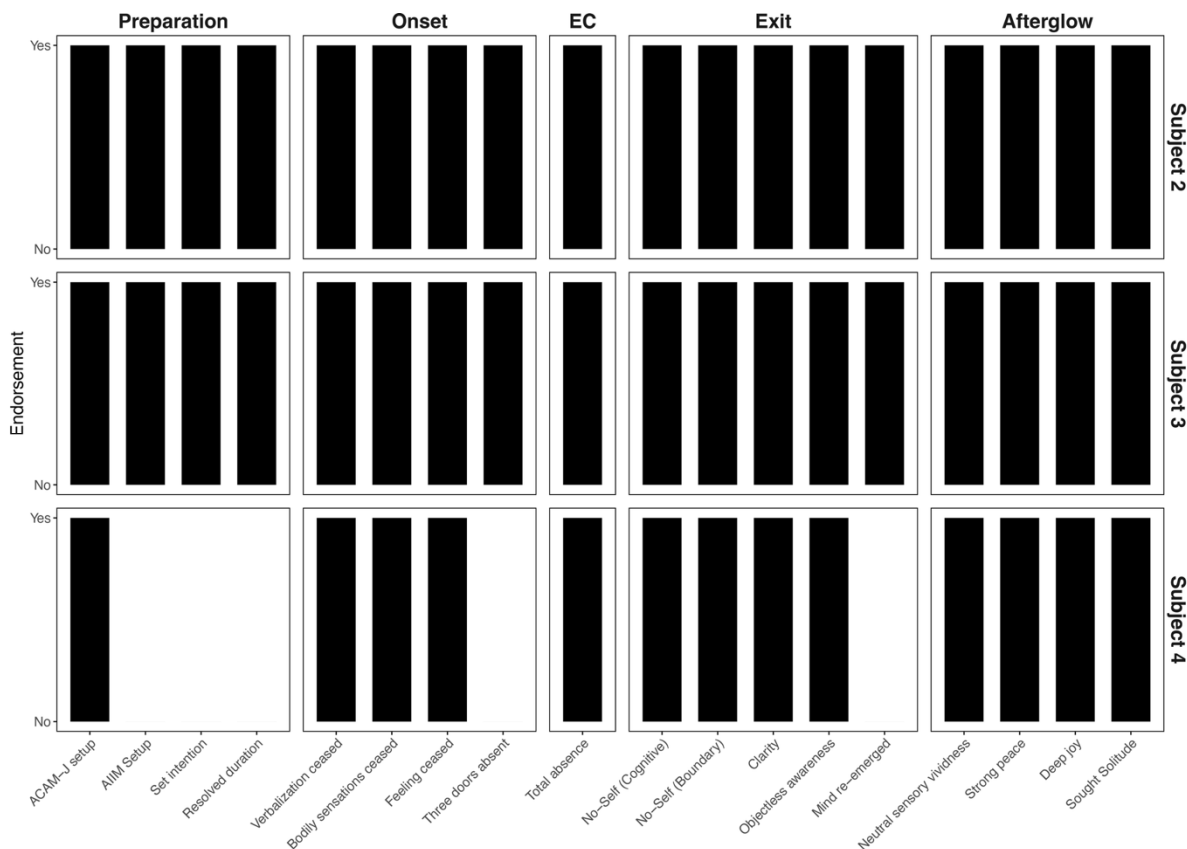
960

961 **Data and materials availability**

962 Data may be requested from the corresponding author and is subject to the Massachusetts
963 General Hospital Institutional Review Board's guidelines and approval. All code used in this
964 study may be made available by request from the corresponding author.

965

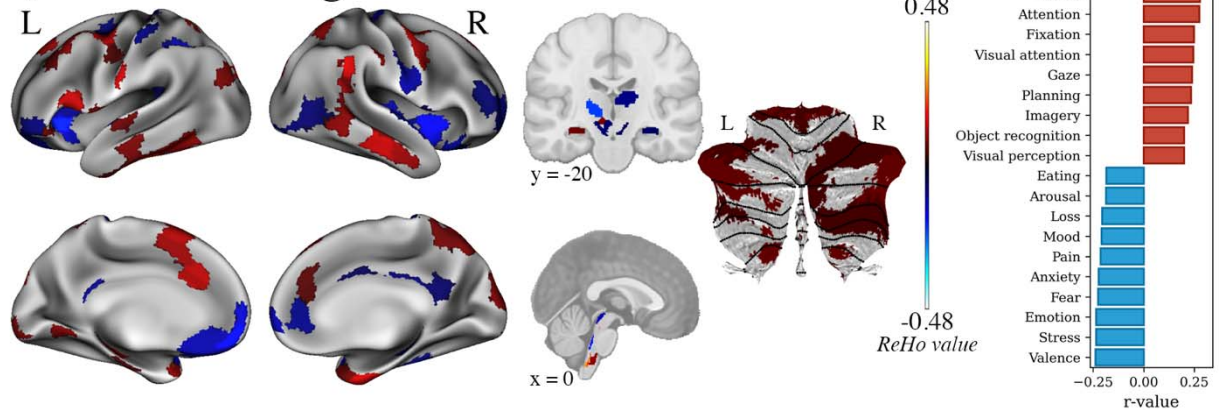
966



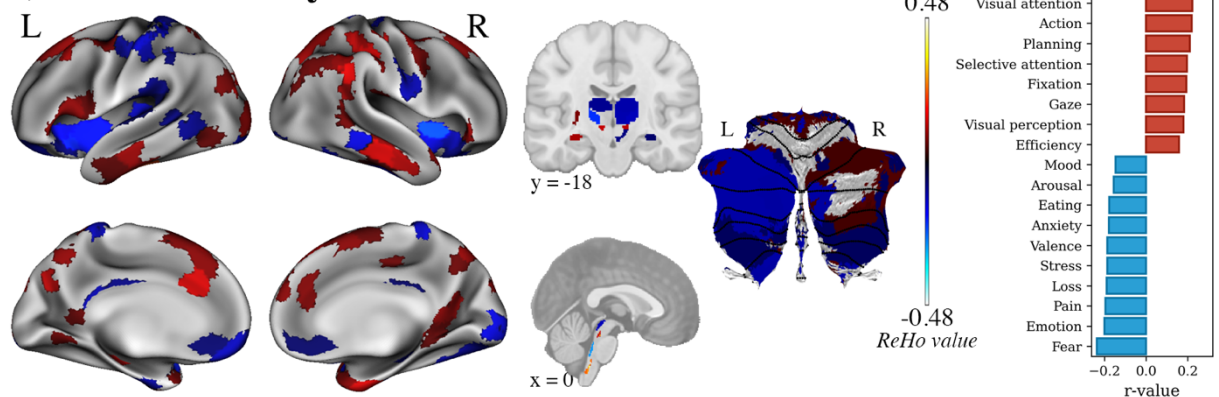
967
968 **Fig. 1. Endorsement of EC phenomenology for each participant.** Participants all endorsed the
969 phenomenological items of EC presented here, except Subject 4. Although previously trained to
970 set up EC using ACAM-J, Subject 4 had since developed an alternative approach and no longer
971 required ACAM-J for setup. As such, the phenomenology for various components throughout
972 EC differ slightly for Subject 4. ACAM-J = Advanced concentration absorption meditation-
973 jhana, AIIM = advanced investigative insight meditation

974

a) EC vs Counting



b) EC vs Memory



975

976

977 **Fig. 2. Differences in regional homogeneity values (ReHo) between EC and control**
 978 **conditions. (a)** EC, compared to the counting control condition, demonstrated increased ReHo
 979 values in the bilateral visual, posterior, temporal regions, parts the brainstem, and cerebellum,
 980 and decreased ReHo in bilateral prefrontal regions and posterior cingulate cortex, largely
 981 associated with the default-mode network. Subcortical activity reveals decreased ReHo values
 982 across the caudate, thalamus, globus pallidus, amygdala, and brainstem. **(b)** Similarly, compared
 983 to the memory condition, EC displayed increased ReHo values in bilateral visual, posterior, and
 984 temporal regions, and decreased ReHo values in the prefrontal and insular regions, and posterior
 985 cingulate cortex. Subcortical regions primarily showed decreased ReHo values spanning the
 986 caudate, thalamus, globus pallidus, hippocampus, amygdala, parts of the brainstem, and
 987 cerebellum. Neurosynth decoding analysis revealed that these patterns of brain activity were
 988 related to cognitive processes associated with perception (e.g., attention, spatial attention, visual

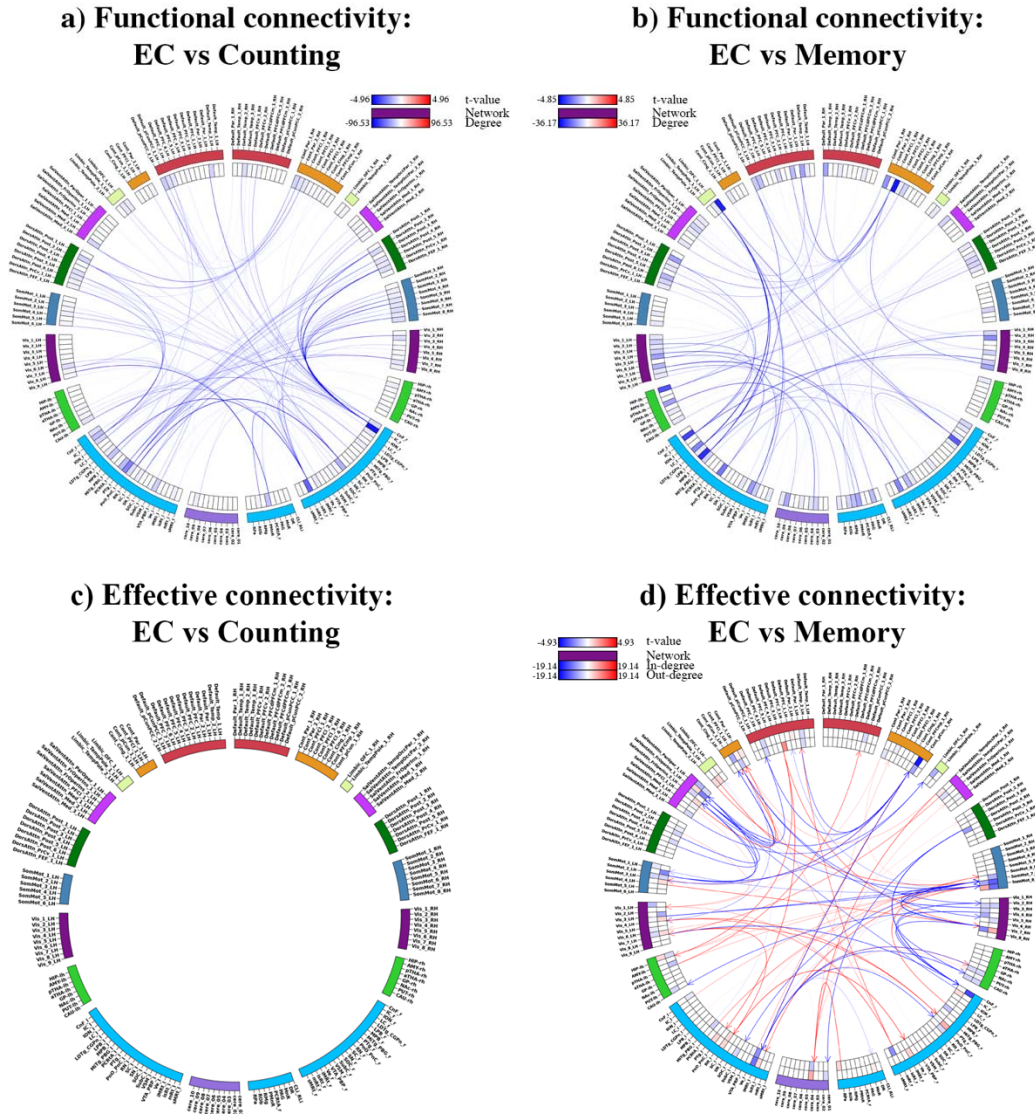
989 attention) and least likely with mental suffering and psychological distress (e.g., fear, stress, loss,
990 pain).

991

992

993

994



995

996 **Fig. 3. Differences in functional connectivity and effective connectivity between EC and**

997 **control conditions.** The figure illustrates (a, b) functional and (c, d) effective connectivity

998 differences between EC and control conditions. Nodes represent brain regions, arranged based on

999 their hemispheric locations and colored according to their network affiliations. For functional

1000 connectivity, lines connecting nodes indicate undirected functional connectivity, with blue

1001 depicting decreased connectivity. Weighted nodal degrees are represented in the heatmap tracks,

1002 depicting the cumulative sum of all its undirected connections. For effective connectivity,

1003 directed connections are displayed using arrowheads, with red lines indicating excitatory

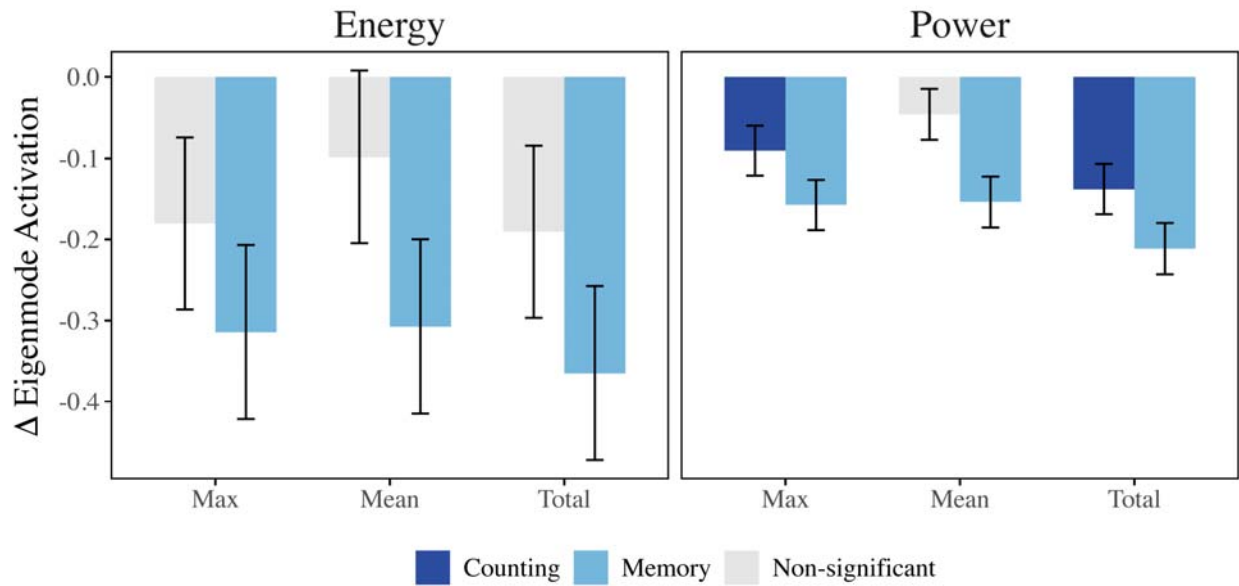
1004 influence from one region to another in EC relative to controls, and blue lines representing
1005 inhibitory influence. Weighted nodal in-degree (incoming connections) and out-degree (outgoing
1006 connections) are also illustrated as heat maps.

1007

1015 gradient values in the highest 30 percentile during EC were distributed among the LN, CN, and
1016 DMN. **(d)** Linear mixed models demonstrated that EC predominantly increases gradient values
1017 in the right parietal, and lower gradient values in the left visual cortex. **(e)** Linear mixed models
1018 demonstrated that EC exhibited higher gradient values in the CN. The red circle on the plot
1019 indicates significance between EC and the control condition. VN = visual network, SMN =
1020 somatomotor network, DAN = dorsal attention network, SN = salience network, LN = limbic
1021 network, CN = control network, DMN = default mode network.

1022

1023



1024

1025 **Fig. 5. Differences in global eigenmode activations between EC and control conditions.**

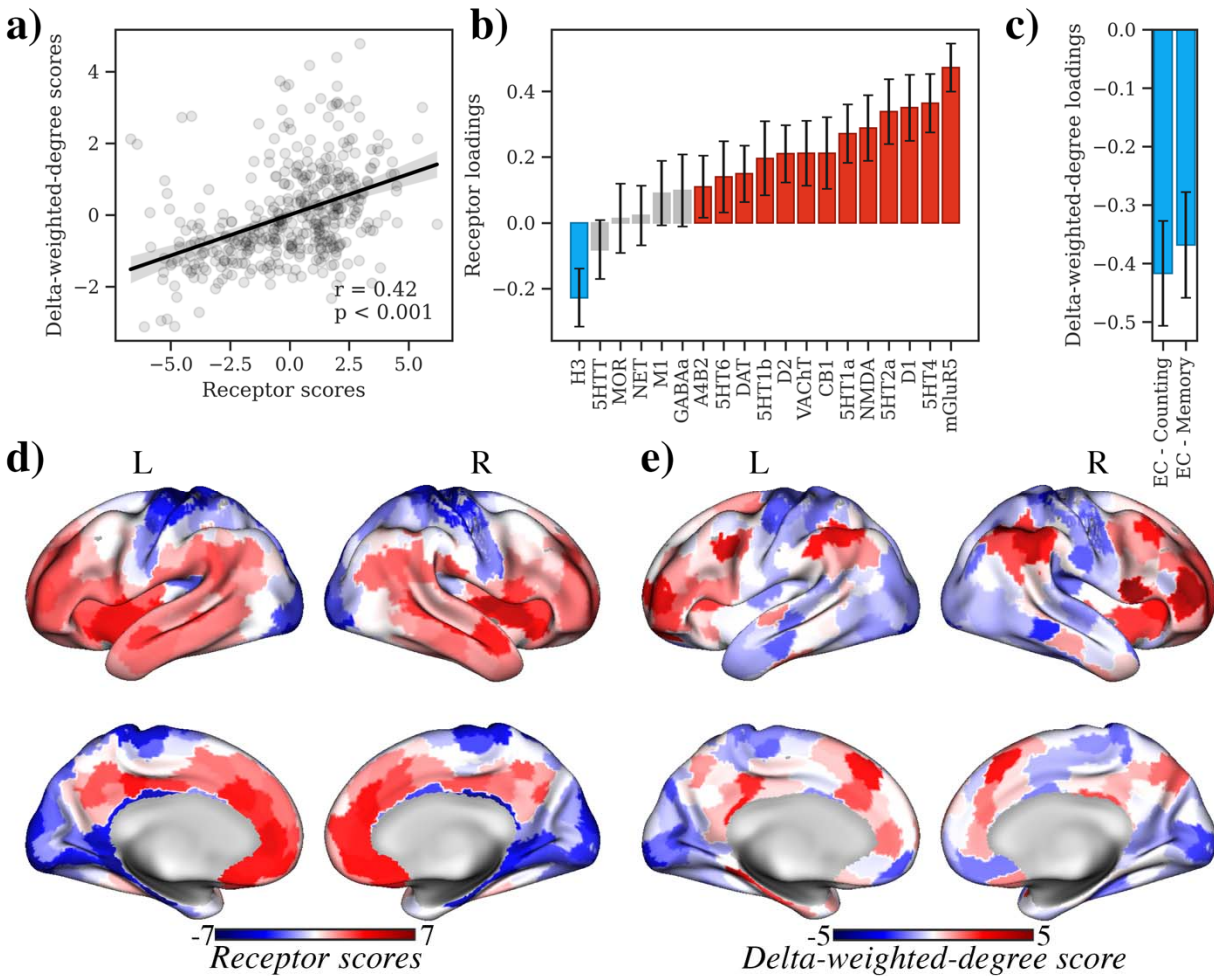
1026 Difference in global eigenmode activation for mean and max energy and power (averaged across

1027 eigenmodes), and total energy and power between EC - counting (dark blue) and EC - memory

1028 (cyan) conditions. Non-significant contrasts are colored grey. Error bars signify standard error.

1029

1030



1031

1032 **Fig. 6. Spatial relationship between brain activity during EC and neurotransmitter**
 1033 **receptor density.** Only partial least squares (PLS) component 1 was significant. (a) Scatter plot
 1034 shows the positive correlation between the latent receptor scores and latent delta-weighted-
 1035 degree scores ($r = 0.42$, $p < 0.001$). (b) The bar chart displays the loadings of different
 1036 neurotransmitter receptors on PLS component 1, with H \square receptors showing negative loadings
 1037 while mGluR $_5$, 5HT $_4$, D1, 5HT $_{2A}$, and NMDA showing positive loadings. (c) The bar chart
 1038 shows the loadings of delta-weighted-degree maps between task conditions, with negative
 1039 loadings on the difference between EC and counting (EC - counting) and memory (EC -
 1040 memory). (d) Spatial distribution of coactivation between receptors ('receptor scores') and (e)
 1041 delta-weighted-degree ('delta-weighted-degree scores'). Red areas indicate regions with positive
 1042 delta-weighted-degree scores, while blue areas represent regions with negative delta-weighted-
 1043 degree scores.